Theoretical Chemistry Accounts (2019) 138:114
https://doi.org/10.1007/s00214-019-2503-5

REGULAR ARTICLE

Computational investigation on the reaction of dimethyl ether with nitric dioxide. I. Underlying mechanism and accurate energetics

Yulei Guan[1] · Ru Liu[1] · Junpeng Lou[1] · Haixia Ma[1] · Jirong Song[1]

Received: 1 April 2019 / Accepted: 29 August 2019 / Published online: 5 September 2019

Abstract
The reaction of dimethyl ether (DME) with nitrogen dioxide (NO_2), which plays a critical role in the low-temperature oxidation behavior of DME, is employed as prototype for reactions of heavier clean ether fuels to assess different hybrid density functionals and "double-hybrid" density functionals. The reaction energies and barrier heights for the reaction system were computed with CCSD(T) theory extrapolated to the complete basis set limit using augmented cc-pVDZ and cc-pVTZ basis sets. The involved energetics were also improved by the CCSD(T)/6-311+G(2df,2p), QCISD(T)/6-311+G(2df,2p), G3B3, G3MP2B3, CBS-QB3, G4, and G4MP2 calculations. It is shown that "double-hybrid" density functionals with the TZVP basis set can give accurate geometries and principal moments of inertia of reactants and products and the B2PLYP/TZVP level can achieve results for barrier heights comparable in accuracy to the high-level ab initio results, which is identified as an important potential theoretical level for direct kinetics studies on the rates of these and homologous reaction systems. The calculated results indicate that NO_2 preferentially captures an out-of-plane hydrogen atom from the DME molecule by the O or the N end via three distinct channels to produce *trans*-HONO, *cis*-HONO, and HNO_2, respectively, and each channel involves the formation of a van der Waals post-reaction adducts lying lower in energy than their separate products.

Keywords Dimethyl ether · Nitrogen dioxide · Hydrogen abstraction · Multi-reference diagnostics · Reaction mechanism · Computational chemistry

1 Introduction

Over the last few decades, there have been increasing searches for clean alternative fuels as well as more efficient combustion strategies for pollutant emission from fossil-based fuel combustion. Ethers, having promising characteristics, are nowadays considered as clean additives blended with conventional internal combustion engine fuels on environmental grounds [1, 2]. Dimethyl ether (DME) is a prototype of such a fuel source for its high cetane number (55–60) and environmentally friendly combustion merits with ultralow emissions of volatile organic compounds, soot, and NO_x—three undesirable exhaust constituents from compression-ignition engines [3]. DME was selected in the present work because it was small enough to allow for a thorough study of its oxidation pathways to achieve the fundamental understanding of the combustion of larger ether fuels.

Even though the automobile engines are fueled by neat ethers, nitrogen dioxide (NO_2) can be produced in considerable amounts by the thermal oxidation of atmospheric nitrogen (N_2) [4]. Several previous investigations have observed that, under combustion conditions, NO_2 would accelerate the combustion rate of the remaining ethers and lower the ignition temperatures, and such an effect became more pronounced as the NO_2 concentration rose, especially in the low-temperature oxidation range [5–7].

To develop the promising DME-fueled engines, the enhancement of NO_2 on the combustion of DME should be clearly explored, and a well-validated DME/NO_2 kinetic model is desired. NO_2, which is an odd-electron species, based on the identified reactions of NO_2 with alkanes [8], is capable of capturing an H atom readily from the DME molecule by the O or the N end to produce *trans*-HONO (channel a), *cis*-HONO (channel b), and HNO_2 (channel c), respectively

$$NO_2 + DME \rightarrow \textit{trans}\text{-HONO} + CH_3OCH_2 \quad \text{(a)}$$

✉ Yulei Guan
guanyl@nwu.edu.cn

[1] School of Chemical Engineering, Northwest University, Xi'an 710069, China

$NO_2 + DME \rightarrow cis\text{-}HONO + CH_3OCH_2$ (b)

$NO_2 + DME \rightarrow HNO_2 + CH_3OCH_2.$ (c)

In this regard, examining the kinetic mechanism of the NO_2 + DME reaction is a valuable step towards capturing the low-temperature behavior and understanding the reaction pathways of the larger ether species to select the next-generation alternative fuels intelligently. However, these three reaction channels have received very little experimental concern and understanding is hampered by the lack of their kinetic data due to the fact that a variety of radical intermediates, especially the NO_2 and CH_3OCH_2 radicals involved in the combustion of DME, are challenging to characterize by experimental approaches before they reach the thermodynamic equilibrium and the presence of inter-conversion of *trans*-HONO, *cis*-HONO, and HNO_2 and their subsequent decomposition to NO + OH rapidly increase the experimental difficulty. There is also the theoretical challenge of whether too much multi-reference character is involved in the NO_2 and transition state structures and single-reference formalisms can reasonably treat the reaction system.

Depending on the discussions above, the main purpose of the present work is particularly to explore each channel mechanism of the DME/NO_2 reaction systematically and give accurate results for the bond energies, reaction energies, and barrier heights of these three reactions. In addition, we attempt to build a computationally affordable electronic compound method utilizing density functional-based considerations, which is then employed in subsequent direct kinetics calculations in the case without apparent reduction of accuracy.

2 Computational methods

All the quantum chemical calculations were carried out using the Gaussian09 computational chemical codes [9]. Ground-state geometries of reactants, products, intermediate, and transition state on the potential energy surfaces of the reaction of DME with NO_2 were completely optimized with the density functionals of BMK [10], MPW1K [11], MPWB1K [12], MPW3LYP [12], wB97X [13], wB97XD [14], M05 [15], M05-2X [16], M06 [17], M06-2X [18], M06HF [18], and M06L [19] with "tight" convergence criteria and "Int = UltraFine". These density functionals except that the wB97X and wB97XD were paired with the TZVP [20] basis set, were coupled with the MG3S [21] basis set. It has been reported that the combinations of BMK, MPW1K, M05-2X, M06L, and M06-2X density functionals with the MG3S basis set could provide accurate thermochemistry and barrier heights for hydrogen-abstraction reactions [22, 23]. The M05 and M06 functionals were adopted in this work due to the fact that they might provide higher accuracy in the cases with large multi-reference character involved. No symmetry restrictions were applied for the calculations. Because NO_2 and CH_3OCH_2, transition states, and post-reaction complexes (IM) were doublet states, all open-shell systems studied here were performed with unrestricted formalism and the calculated results were assessed for wave-function instability, while the spin-restricted formalism was used in the DME, *trans*-HONO, *cis*-HONO, and HNO_2 singlet-state calculations.

In addition, "double-hybrid" density functionals (including B2PLYP [24], B2PLYPD [25], B2PLYPD3 [26, 27], mPW2PLYP [28], and mPW2PLYPD [25]) in conjunction with the TZVP basis set have also been employed to characterize the reaction of DME with NO_2.

Harmonic vibrational frequency analyzes of the located stationary points, calculated at the same level, were performed partly to confirm that the optimized structures were located at minima or transition states on the potential energy surfaces and partly to obtain the zero-point vibrational energy (ZPVE) and the thermal contributions to the enthalpy and free energy. Transition states corresponded to the first-order saddle points characterized by a single imaginary frequency which confirmed the process of the abstraction of an H atom from DME and a transfer to the O or the N end of NO_2. Furthermore, intrinsic reaction coordinate (IRC) computations [29, 30] in both forward and backward directions with a step size of 0.04 bohr were also performed to verify that the identified transition states with products and reactants were correctly connected.

A variety of coupled cluster approximations were used to compute single-point electronic energies for the optimized stationary points with the aforementioned theoretical levels. The coupled cluster approximations used in this work were as follows: coupled cluster theory with single and double substitutions, CCSD [31, 32] and QCISD [33]; coupled cluster theory with single and double excitations and a quasiperturbative treatment of connected triple excitations, CCSD(T) [34] and QCISD(T) [33, 34]. In the cases of CCSD, CCSD(T), QCISD, and QCISD(T) calculations, augmented correlation-consistent aug-cc-pVDZ and aug-cc-pVTZ basis sets [35–37] have been used and extrapolated to the complete basis set limit. To reach the CBS limit, we have used coefficients recommended by Schwenke [38] in two-point extrapolation schemes involving the aug-cc-pVDZ and aug-cc-pVTZ basis sets.

We have also used the G3B3 [39], G3MP2B3 [39], CBS-QB3 [40], G4 [41], and G4MP2 [42] composite methods to evaluate the involved energetics of the NO_2 + DME reaction. Specifically, the post-reaction complex calculations were performed by taking the counterpoise correction for basis set superposition error (BSSE) [43] into account.

3 Results and discussion

3.1 Multi-reference diagnostics

Before characterizing the reaction of DME with NO_2 with different single-determinant reference formalisms, it is much necessary to evaluate whether such methods are reasonable above all. The T1 [44], GB1 [16, 45], and %TAE[T] [46] diagnostic approaches were employed here to measure multi-reference extent in the wave function of the involved species.

The T1 diagnostic provides a qualitative assessment of the extent of multi-reference feature by examining the amplitudes from single excitations in the CCSD calculations. It has been mentioned that the presence of large single amplitudes in a specific species was debatable, and the T1 value over ca. 0.02 for a closed-shell species suggested that significant multi-reference character was involved in its wave function [44]. With regard to the open-shell species, several previous studies [47–50] have suggested that threshold for the T1 values up to ca. 0.045 could be more reasonable. The T1 diagnostic results performed on the M06-2X/MG3S, B2PLYP/TZVP, and wB97XD/TZVP optimized reactants, products, post-reaction adducts, and transition states of reaction channels R(a)–R(c) are outlined in Table 1. Most of the open-shell species (NO_2, CH_3OCH_2, TSb, TSc, IMa, IMb, and IMc) involved in the reactions R(a)–R(c) do not possess substantial multi-reference character, but TSa has a T1 value between 0.037 and 0.042, depending on the method adopted, which approaches the upper limit of 0.045, showing multi-reference warning sign. T1 diagnostic for the closed-shell species DME is calculated to be significantly smaller than the threshold of 0.02, whereas those for the three HNO_2 isomers are very close to the threshold of 0.02. The above T1 diagnostic calculations suggest that the single-reference treatments seem suitably to describe the NO_2 + DME reaction, despite the critical problems related with the transition state TSa.

However, some previous investigations [45, 51, 52] have concluded that the T1 diagnostic was not completely reliable. Consequently, the (G)B1 and %TAE[(T)] diagnostic methods were also employed to evaluate the multi-reference features for the NO_2 + DME reaction system.

Truhlar et al. [16, 45] proposed the GB1 diagnostic procedure, a more computationally affordable alternative compared to the T1 diagnostic, by evaluating the extent of multi-reference feature associated with energetics. The GB1 diagnostic is an improved level of the B1 diagnostic where the absolute difference in zero-point-exclusive bond energies calculated with the BLYP (no Hartree–Fock exchange) and B1LYP (25% of Hartree–Fock exchange) functionals based on the BLYP geometries in both cases plays the part of the predictor of multi-reference feature. The discrepancy over ca. 41.84 kJ mol^{-1} in energy between the results of these two functionals implies the presence of significant multi-reference feature. Table 2 lists the B1 diagnostic values for the four bond dissociation energies and the GB1 diagnostic values for the three reaction energies, three forward activation barriers, and three reverse activation barriers for these three reaction channels in the present work.

It can be concluded from the B1 and GB1 diagnostic values in Table 2 that all of the breaking and forming bonds involved in the three reaction channels and the reaction energies for reactions R(a), R(b), and R(c) are appropriate for treatments using single-reference formalisms: the B1/GB1 diagnostic quantities for all of these three reaction pathways are substantially lower than the threshold of 41.84 kJ mol^{-1} for significant multi-reference feature. In addition, the GB1 values for forward and reverse barrier heights are appreciably larger than those for bond and reaction energies, and an encouraging sign of consistency between the T1 and GB1 diagnostic is that T1 diagnostic value for TSa is large, and we find the forward and reverse barrier heights of R(a) also have large GB1 diagnostics.

Table 1 T1 diagnostics for species involved in the reaction of DME with NO_2

Species	CCSD/cc-pVDZ			CCSD/cc-pVTZ			CCSD/aug-cc-pVDZ			CCSD/aug-cc-pVTZ		
	M062X	B2PLYP	wB97XD	M062X	B2PLYP	wB97XD	M062X	B2PLYP	wB97XD	M062X	B2PLYP	wB97XD
CH_3OCH_3	0.009	0.009	0.009	0.009	0.010	0.009	0.011	0.011	0.011	0.010	0.010	0.010
NO_2	0.023	0.024	0.023	0.023	0.024	0.023	0.024	0.026	0.025	0.024	0.025	0.024
TSa	0.037	0.041	0.037	0.037	0.041	0.038	0.038	0.042	0.038	0.037	0.041	0.038
TSb	0.029	0.031	0.027	0.028	0.030	0.027	0.029	0.030	0.028	0.028	0.030	0.027
TSc	0.021	0.022	0.021	0.021	0.021	0.021	0.022	0.022	0.022	0.021	0.022	0.021
IMa	0.019	0.020	0.019	0.018	0.020	0.019	0.020	0.021	0.020	0.019	0.020	0.019
IMb	0.019	0.020	0.020	0.019	0.020	0.020	0.020	0.021	0.021	0.020	0.020	0.020
IMc	0.018	0.019	0.019	0.018	0.019	0.018	0.019	0.020	0.020	0.018	0.019	0.019
CH_3OCH_2	0.015	0.015	0.015	0.015	0.015	0.015	0.017	0.017	0.017	0.016	0.016	0.016
trans-HONO	0.019	0.021	0.019	0.019	0.020	0.019	0.021	0.022	0.021	0.019	0.021	0.020
cis-HONO	0.020	0.021	0.020	0.019	0.020	0.019	0.021	0.022	0.021	0.020	0.021	0.020
HNO_2	0.019	0.020	0.019	0.018	0.019	0.018	0.020	0.021	0.020	0.019	0.020	0.019

Table 2 Bond energies, reaction energies, barrier heights, B1 diagnostics, and GB1 diagnostics in kJ mol^{-1}

Properties	BLYP/MG3S	B1LYP/MG3S	(G)B1 diagnostic
$D_e(H–CH_2OCH_3)$	411.17	415.63	4.46
$D_e(H_3C–OCH_3)$	338.93	344.82	4.11
D_e(*trans*-H–ONO)	328.05	332.18	4.12
D_e(*cis*-H–ONO)	322.17	330.49	8.32
$D_e(H–NO_2)$	300.35	309.08	8.73
ΔE[R(a)]	83.11	83.45	0.34
ΔE[R(b)]	89.00	85.14	3.86
ΔE[R(c)]	110.82	106.55	4.27
$\Delta_r E_a$[R(a)]	98.82	123.32	24.50
$\Delta_r E_a$[R(b)]	78.92	89.39	10.46
$\Delta_r E_a$[R(c)]	85.87	93.48	7.61
$\Delta_r E_a$[R(a)]	33.87	58.94	25.06
$\Delta_r E_a$[R(b)]	9.66	23.54	14.49
$\Delta_r E_a$[R(c)]	0.80	7.86	7.07

The %TAE[(T)] multi-reference diagnostic [46] is performed by calculating the percentage of the CCSD(T) total atomization energy (TAE) that comes from the (T) correction and is given by

$$\%\mathrm{TAE[(T)]} = \frac{|\mathrm{TAE[CCSD(T)]} - \mathrm{TAE[CCSD]}|}{\mathrm{TAE[CCSD(T)]}} \quad (1)$$

The %TAE[(T)] calculated values can be divided into four grades in a qualitative level: the %TAE[(T)] values (1) less than 2% suggest dynamical correlations are largely dominant in the systems; (2) ranging from 2 to ~ 4–5% imply weak nondynamical correlation; (3) in the range from ~ 4 to 5% to about ~ 10% imply modest nondynamical correlation; and (4) above 10% indicate strong nondynamical correlation. The aug-cc-pVTZ basis set was adopted through the %TAE[(T)] diagnostic procedure.

Table 3 collects the %TAE[(T)] diagnostic results for the optimized geometries at the M06-2X/MG3S, B2PLYP/TZVP, and wB97XD/TZVP levels. These data in Table 3 suggest that all of the species in the three reaction channels are suitable for investigations with single-reference methods as well: the %TAE[(T)] diagnostics for all involved species are lower than 10%.

Depending on the three multi-reference diagnostic analyses, especially the (G)B1 and %TAE[(T)] diagnostics, it can be argued that single-reference formalisms can be employed to adequately describe the NO_2 + DME reaction system.

3.2 Geometries

In this regard, we are focusing on the performance of these adopted density functionals in the optimizations of the ground-state geometries of the reactants and products

Table 3 %TAE[(T)] diagnostic

Species	%TAE[(T)]		
	M062X	B2PLYP	wB97XD
CH_3OCH_3	1.34	1.30	1.30
NO_2	8.16	8.59	8.26
TSa	3.29	2.99	3.26
TSb	3.04	3.06	3.02
TSc	3.06	3.12	3.07
IMa	2.64	2.73	2.68
IMb	2.65	2.73	2.68
IMc	2.82	2.92	2.86
CH_3OCH_2	1.42	1.43	1.42
trans-HONO	5.20	5.50	5.27
cis-HONO	5.21	5.45	5.27
HNO_2	5.90	6.17	5.96

involved in R(a), R(b), and R(c). Especially, the discrepancies between the principal moments of inertia of the ground-state geometries and the calculated equilibrium ones are interested, because the rotational partition functions, which are required by the rate constant calculations, are derived using these aforementioned quantities.

Figure 1 depicts the optimized geometries of the reactants and products of reactions R(a), R(b), and R(c). Selected geometrical parameters and products of the principal moments

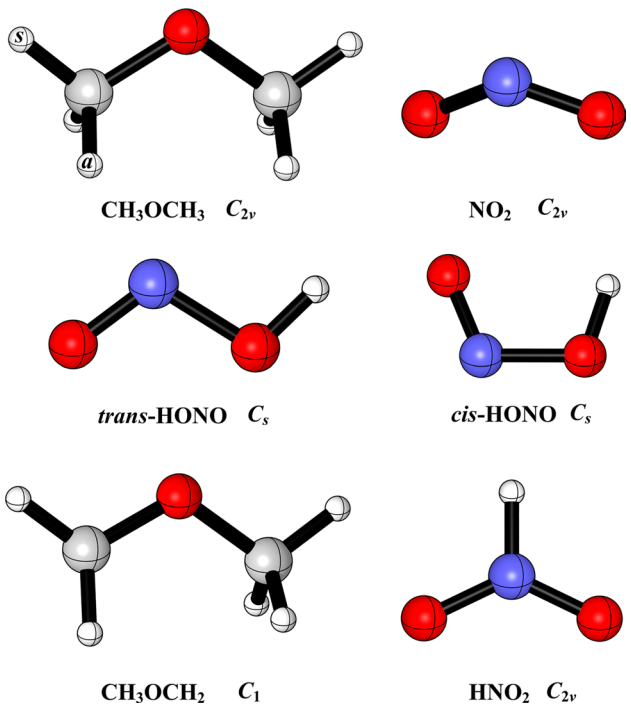

Fig. 1 Reactants and products for reaction of DME with NO_2. Color coding of atoms: red, oxygen; blue, nitrogen; gray, carbon; and white, hydrogen

Table 4 Comparison of DFT and experimental geometries for reactants and products of reaction of DME with NO_2

Species	Parameter[a]	Experiment	BMK	M052X	M05	M062X	M06	M06L	B2PLYP	B2PLYPD	mPW2PLYP	mPW2PLYPD	wB97XD
DME	R(C–O)	1.411	1.397	1.407	1.397	1.402	1.395	1.401	1.412	1.412	1.408	1.408	1.402
	R(C–H_s)	1.085	1.089	1.084	1.088	1.087	1.089	1.087	1.087	1.088	1.086	1.086	1.089
	R(C–H_a)	1.099	1.099	1.092	1.097	1.096	1.099	1.097	1.097	1.097	1.095	1.096	1.099
	A(C–O–C)	111.2	112.8	111.6	113.6	112.0	111.9	111.8	111.8	111.4	112.0	111.7	112.3
	A(H_s–C–O)	107.1	107.8	107.7	107.6	107.8	108.2	107.8	107.4	107.4	107.4	107.5	107.6
	A(H_a–C–O)	111.0	111.4	110.9	111.6	111.1	111.5	111.7	111.4	111.3	111.4	111.3	111.6
	A(H_s–C–H_a)	109.2	108.9	109.3	108.8	109.1	108.8	108.8	109.0	109.2	109.0	109.1	108.9
	A(H_a–C–H_a)	108.0	108.3	108.7	108.2	108.5	107.9	107.9	108.5	108.5	108.5	108.4	108.3
	$I_A I_B I_C$	37,234	35,384	35,956	35,466	35,722	35,073	35,782	36,872	36,853	36,412	36,399	35,981
NO_2	R(N–O)	1.193	1.191	1.178	1.183	1.180	1.183	1.193	1.201	1.201	1.196	1.196	1.185
	A(O–N–O)	134.1	134.5	135.2	135.1	135.0	134.8	134.3	133.8	133.8	134.1	134.1	134.3
	$I_A I_B I_C$	3364	3238	2969	3052	3015	3074	3294	3479	3479	3368	3368	3166
trans-HONO	R(N–O)	1.442	1.395	1.388	1.402	1.387	1.403	1.441	1.446	1.446	1.430	1.430	1.403
	R(N–O)	1.169	1.169	1.159	1.162	1.161	1.160	1.165	1.169	1.169	1.167	1.167	1.163
	R(O–H)	0.959	0.964	0.963	0.965	0.965	0.966	0.967	0.969	0.969	0.967	0.967	0.965
	A(O–N–O)	110.6	111.1	111.2	111.2	111.0	111.1	110.8	111.1	111.1	111.2	111.2	111.2
	A(H–O–N)	102.1	103.8	103.9	103.3	103.9	103.3	102.2	102.0	102.0	102.4	102.4	103.0
	$I_A I_B I_C$	10,070	9127	8775	9118	8804	9106	10,012	10,215	10,218	9814	9815	9160
cis-HONO	R(N–O)	1.399	1.368	1.359	1.367	1.360	1.368	1.398	1.400	1.401	1.389	1.389	1.369
	R(N–O)	1.186	1.181	1.171	1.174	1.172	1.173	1.178	1.184	1.184	1.181	1.181	1.175
	R(O–H)	0.989	0.974	0.973	0.976	0.975	0.978	0.978	0.980	0.980	0.978	0.978	0.976
	A(O–N–O)	113.6	113.6	113.5	114.1	113.6	113.7	113.7	113.4	113.5	113.5	113.5	113.5
	A(H–O–N)	103.9	106.8	106.5	106.7	106.8	106.2	105.9	105.5	105.7	105.8	105.9	106.4
	$I_A I_B I_C$	10,255	9579	9174	9420	9227	9402	10,141	10,336	10,355	10,010	10,021	9489
MUE	R	–	0.95%	1.30%	1.09%	1.27%	1.10%	0.42%	0.36%	0.37%	0.50%	0.49%	0.99%
MUE	A	–	0.82%	0.75%	0.93%	0.76%	0.70%	0.47%	0.43%	0.38%	0.48%	0.44%	0.66%
MUE	$I_A I_B I_C$	–	6.17%	9.64%	7.90%	9.26%	8.08%	1.92%	1.66%	1.72%	1.81%	1.79%	6.44%

[a]Bond lengths are in Å, bond and dihedral angles are in degrees, and products of principal moments of inertia are in amu^3 Å^6

Table 5 Selected DFT imaginary frequencies (Imag) and geometries for transition states of reactions R(a), R(b), and R(c)

TSa				TSb				TSc			
Parameter[a]	M062X	B2PLYP	wB97XD	Parameter	M062X	B2PLYP	wB97XD	Parameter	M062X	B2PLYP	wB97XD
Imag	1389*i*	1254*i*	1189*i*	Imag	1506*i*	1524*i*	1530*i*	Imag	1592*i*	1598*i*	1530*i*
R(C1–O1)	1.358	1.366	1.358	*R*(C1–O1)	1.351	1.358	1.349	*R*(C1–O1)	1.347	1.357	1.348
R(C1–H1)	1.087	1.087	1.088	*R*(C1–H1)	1.087	1.087	1.088	*R*(C1–H1)	1.085	1.085	1.087
R(C1–H2)	1.205	1.198	1.211	*R*(C1–H2)	1.301	1.349	1.337	*R*(C1–H2)	1.415	1.454	1.434
R(C1–H3)	1.095	1.095	1.096	*R*(C1–H3)	1.092	1.092	1.094	*R*(C1–H3)	1.092	1.092	1.094
R(C2–O1)	1.417	1.430	1.419	*R*(C2–O1)	1.417	1.431	1.420	*R*(C2–O1)	1.421	1.433	1.422
R(C2–H4)	1.085	1.085	1.087	*R*(C2–H4)	1.085	1.085	1.087	*R*(C2–H4)	1.085	1.085	1.087
R(C2–H5)	1.092	1.090	1.092	*R*(C2–H5)	1.091	1.090	1.092	*R*(C2–H5)	1.090	1.090	1.092
R(C2–H6)	1.091	1.092	1.094	*R*(C2–H6)	1.092	1.092	1.094	*R*(C2–H6)	1.092	1.092	1.094
R(O2–H2)	1.414	1.439	1.409	*R*(O2–H2)	1.293	1.250	1.260	*R*(N–H2)	1.254	1.228	1.240
R(O2–N)	1.292	1.310	1.305	*R*(O2–N)	1.272	1.305	1.283	*R*(O2–N)	1.199	1.220	1.204
R(O3–N)	1.189	1.208	1.192	*R*(O3–N)	1.192	1.209	1.196	*R*(O3–N)	1.203	1.224	1.209
A(H1–C1–O1)	110.4	109.7	110.0	*A*(H1–C1–O1)	110.8	110.5	110.8	*A*(H1–C1–O1)	111.9	111.3	111.5
A(H1–C1–H2)	105.7	105.0	104.7	*A*(H1–C1–H2)	101.4	100.4	100.6	*A*(H1–C1–H2)	102.3	102.0	102.2
A(H1–C1–H3)	113.7	113.6	113.7	*A*(H1–C1–H3)	115.0	115.3	115.1	*A*(H1–C1–H3)	116.1	116.2	116.0
A(H3–C1–O1)	114.2	114.2	114.5	*A*(H3–C1–O1)	115.0	115.3	115.5	*A*(H3–C1–O1)	115.8	115.9	116.0
A(H2–C1–O1)	108.2	109.4	109.5	*A*(H2–C1–O1)	110.5	111.1	110.7	*A*(H2–C1–O1)	107.1	108.2	108.0
A(C1–O1–C2)	114.1	114.6	114.8	*A*(C1–O1–C2)	115.3	115.2	115.5	*A*(C1–O1–C2)	115.0	115.0	115.3
A(C1–H2–O2)	166.2	170.9	171.6	*A*(C1–H2–O2)	174.7	172.2	173.2	*A*(C1–H2–N)	171.9	175.9	175.0
A(H2–O2–N)	101.3	101.6	102.1	*A*(H2–O2–N)	109.3	110.9	110.9	*A*(H2–N–O2)	117.4	117.0	117.0
A(O2–N–O3)	115.7	116.2	115.0	*A*(O2–N–O3)	118.6	117.7	118.0	*A*(O2–N–O3)	128.2	127.6	127.7
D(H4–C2–O1–C1)	− 175.7	− 178.4	179.6	*D*(H4–C2–O1–C1)	176.6	178.1	179.2	*D*(H4–C2–O1–C1)	− 179.0	− 175.0	− 176.0
D(C2–O1–C1–H2)	75.6	79.4	77.8	*D*(C2–O1–C1–H2)	81.5	83.5	82.6	*D*(C2–O1–C1–H2)	− 78.9	− 77.3	− 76.7
D(O1–C1–H2–O2)	7.3	13.4	10.9	*D*(O1–C1–H2–O2)	145.2	141.0	138.2	*D*(O1–C1–H2–N)	14.6	21.8	22.0
D(C1–H2–O2–N)	11.3	− 5.5	− 3.9	*D*(C1–H2–O2–N)	140.9	155.6	154.4	*D*(C1–H2–N–O2)	− 162.4	− 166.2	− 164.5
D(H2–O2–N–O3)	178.9	177.8	178.0	*D*(H2–O2–N–O3)	1.6	1.3	1.6	*D*(C1–H2–N–O3)	17.4	14.0	15.7
$I_A I_B I_C$	7,153,237	8,356,986	8,058,025	$I_A I_B I_C$	6,748,392	7,349,840	7,068,626	$I_A I_B I_C$	7,792,240	8,692,138	8,278,617

[a]Imaginary frequencies are in cm^{-1}, Bond lengths are in Å, bond and dihedral angles are in degrees, and products of principal moments of inertia are in amu^3 $Å^6$

of inertia obtained with various DFT-based electronic model chemistries used in this study are compared in Table 4 with the experimental data. The last three lines in Table 4 correspond to the mean unsigned errors (MUEs) of calculated bond lengths, bond angles, and products of the principal moments of inertia with respect to experimental data. The latest version of Computational Chemistry Comparison and Benchmark Database [53] (http://cccbdb.nist.gov/) provides the experimental results for the geometries and products of the principal moments of inertia for the involved species except CH_3OCH_2 and HNO_2.

As can be seen from Table 4 that the equilibrium structures optimized by the different density functionals except the M06HF/MG3S level match very well with their experimental results for ground-state geometries, even for the strongly non-rigid NO_2 geometry, leading MUEs by 0.36–1.27% to the bond lengths (R), 0.38–0.82% to the bond angles (A), and 1.66–9.26% to the products of the principal moments of inertia ($I_A I_B I_C$). In particular, the computed equilibrium geometries and products of the principal moments of inertia by the "double-hybrid" density functionals, especially the B2PLYP/TZVP level with the smallest mean unsigned errors, achieve the best agreement with the experimental data.

As can be seen from Fig. 1 and Table 4, complete optimizations of DME, NO_2, *trans*-HONO, *cis*-HONO, and HNO_2 ultimately lead to C_{2v}, C_{2v}, C_s, C_s, and C_{2v} symmetries, respectively. There are two equivalent C–O bonds but two different H atom distributions in the DME geometry. Because the two in-plane C–H_s bonds appear to be a little shorter than the four out-of-plane C–H_a bonds, it can be argued that NO_2 prefers to attack the out-of-plane H_a in the hydrogen-abstraction process. In addition, we can observe that the two in-plane H_s atoms eclipse the central O atom with the bending angle being ca. 112°.

Removing an out-of-plane H_a atom from DME by the O or the N end of NO_2 to form *trans*-HONO (channel a), *cis*-HONO (channel b), and HNO_2 (channel c), respectively, requires to get over the transition states TSa, TSb, and TSc which are directly connected to the post-reaction adducts IMa, IMb, and IMc. Vibrational frequency analysis of TSa, TSb, and TSc confirms the presence of a single imaginary frequency (Imag), as listed in the first line of Table 5. Here note that unsuccessful attempts were made to locate a transition structure for NO_2 capturing the in-plane H_s atoms using various levels of theory. The identified geometries of the transition states for the three DME reactions are depicted in Fig. 2 and given in Table 5 in detail. The three transition structures account for the lowest energy torsional conformations by optimizations with all the DFT-based electronic model chemistries used in this work. The geometries of reactants, products, and the transition states computed with the various DFT-based electronic model chemistries are very similar except that the transition states cannot be located by the M06HF/MG3S level. In order to avoid being redundant, the following discussions are only based on the geometrical parameters optimized with the M06-2X/MG3S, B2PLYP/TZVP, and wB97XD/TZVP levels, which are used in all single-point calculations throughout this work. In addition, the B2PLYP/TZVP calculations will be used in the kinetics study of the title reaction.

For the TSa structure optimized at the M06-2X/MG3S level, the C···H bond being broken is stretched by only 9.94% as compared to that in DME, while the length of the O···H bond being formed in TSa is 1.414 Å, 44.73% longer than its value in equilibrium structure of IMa, indicative of a quite reactant-like character. Both the B2PLYP/TZVP and wB97XD/TZVP levels qualitatively reproduce the same trend, and the B2PLYP/TZVP level gives an even earlier character to TSa compared to the M06-2X/MG3S results. For the R(b) process calculated at the M06-2X/MG3S level, the C···H bond being broken is lengthened by

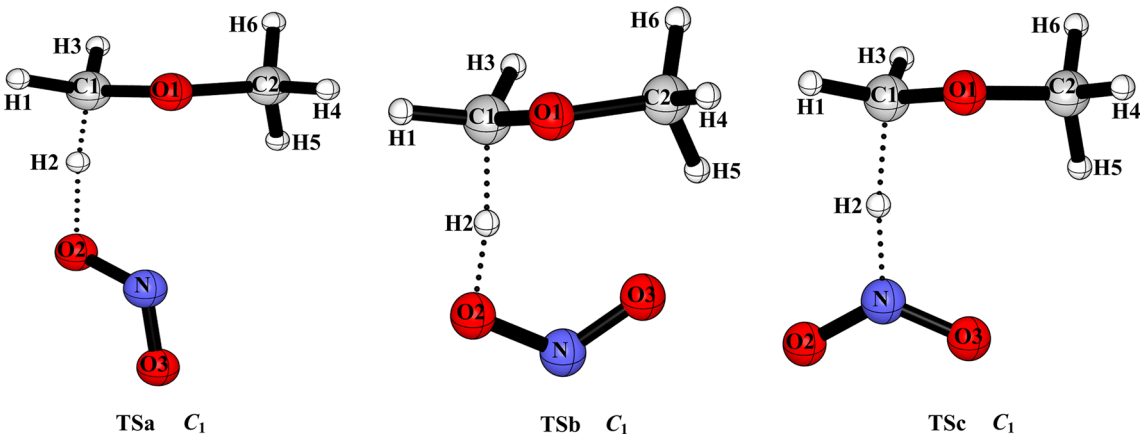

Fig. 2 Transition states for the three reaction channels of DME with NO_2

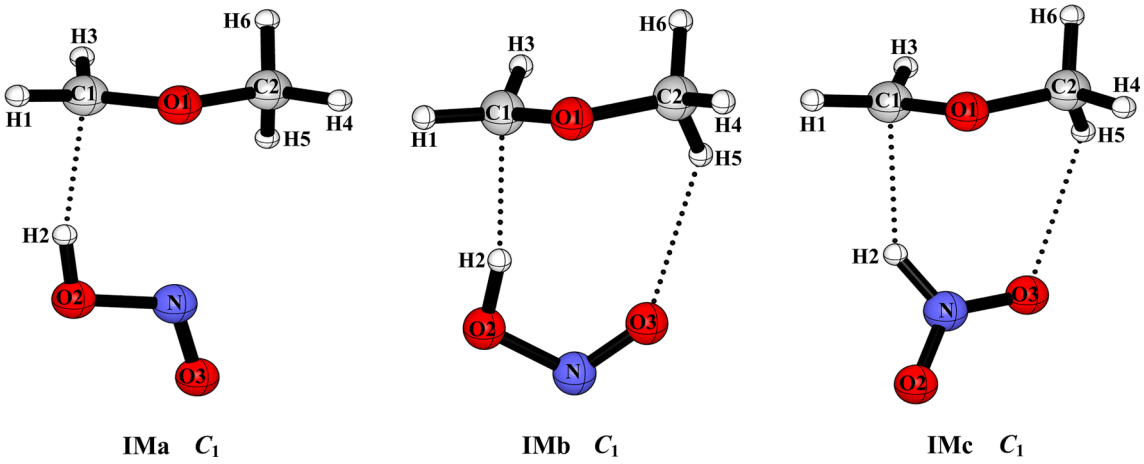

Fig. 3 Post-reaction adducts for the three reaction channels of DME with NO_2

18.70% to reach the TSb transition structure (1.301 Å) from DME (1.096 Å), whereas the length of the O···H bond being formed in TSb is 1.293 Å, 30.74% longer than that (0.989 Å) of IMb, implying that TSb also possesses a reactant-like character, but is slightly "later" than TSa. Similar conclusion follows from the calculated results of other adopted levels. By comparing the optimized DME, TSc, and IMc structures listed in Table 5, we can see that TSc is located to be product-like. Depending on the above geometrical parameters of TSa, TSb, and TSc, it leads to the conclusion that reactions R(a) and R(b) should be exothermic, while reaction R(c) should be endothermic based on the Hammond's postulate—transition states are located towards the higher energy side, and the activation barriers for the three forward reaction channels would be in the $\Delta_f E_a[\mathrm{R(a)}] < \Delta_f E_a[\mathrm{R(b)}] < \Delta_f E_a[\mathrm{R(c)}]$ order.

The IRC outcomes clearly show that, on the reactant side, transition states connect to the $NO_2 + DME$ minimum-energy geometry with almost equal energy to the separate reactants; on the product side, the IRC evolutions of the three reaction channels vary with the formations of the hydrogen-bonded post-reaction complexes (see Fig. 3; Table 6 for detailed structures of IMa, IMb, and IMc) instead of the free products. One can observe that there are great geometrical similarity between the located post-reaction adducts and the separate products. In addition, the distances between the C atom of CH_2 moiety in CH_3OCH_2 and the H atom of *trans*-HONO, *cis*-HONO, and HNO_2 in the IMa, IMb, and IMc structures, are predicted at the B2PLYP/TZVP level to be 2.106, 2.121, and 2.093 Å, respectively. The distance from the H5 atom of CH_3 moiety in CH_3OCH_2 to the O3 atom of *cis*-HONO in IMb and HNO_2 in IMc is predicted to be 2.625 and 2.669 Å at the B2PLYP/TZVP level, respectively, indicating presences of a weak hydrogen-bonding interaction.

3.3 Zero-point energies

Table 7 presents the comparison of the computed zero-point energies (ZPEs) for the reactants and products of reactions R(a), R(b), and R(c) with the experimental ones. The DFT ZPEs presented in Table 7 are corrected by the scaling factors which have values of 0.971 for BMK/MG3S, 0.962 for M05-2X/MG3S, 0.977 for M05/MG3S, 0.970 for M06-2X/MG3S, 0.981 for M06/MG3S, 0.978 for M06L/MG3S, 0.982 for MPW3LYP/MG3S, 0.956 for MPW1K/MG3S, 0.954 for MPWB1K/MG3S, 0.970 for wB97X/TZVP, 0.975 for wB97XD/TZVP, 0.9832 for B2PLYP/TZVP, respectively [54, 55]. The present study improves the B2PLYPD/TZVP, mPW2PLYP/TZVP, and mPW2PLYPD/TZVP ZPEs by multiplying the same factors as that for the B2PLYP/TZVP-based ZPEs.

The scaled computed ZPEs are in good accord with experiment for the electronic model chemistries examined here, with MUEs in the range of 0.97–2.70 kJ mol^{-1}. The best performance in the case of ZPEs is M06L/MG3S. We note that the B2PLYP/TZVP theoretical level, which will be used in the future kinetics calculations, also performs reasonably well with respect to the experimentally based ZPEs, with respective MUE by 1.17 kJ mol^{-1}. The scaled ZPEs of the lowest energy transition state structures and post-reaction adducts structures for the three DME reactions are also included in Table 7.

3.4 Zero-point-corrected activation barrier heights

Adding the ZPE difference between each transition state and the reactants to the zero-point-exclusive barrier heights yields the zero-point-corrected barrier heights for reactions

Table 6 Selected DFT geometries for intermediates of reactions R(a), R(b), and R(c)

IMa				IMb				IMc			
Parameter[a]	M062X	B2PLYP	wB97XD	Parameter	M062X	B2PLYP	wB97XD	Parameter	M062X	B2PLYP	wB97XD
R(C1–O1)	1.339	1.349	1.341	*R*(C1–O1)	1.340	1.350	1.342	*R*(C1–O1)	1.341	1.349	1.340
R(C1–H1)	1.080	1.080	1.082	*R*(C1–H1)	1.080	1.080	1.083	*R*(C1–H1)	1.080	1.080	1.083
R(C1–H2)	2.135	2.106	2.043	*R*(C1–H2)	2.152	2.121	2.062	*R*(C1–H2)	2.203	2.093	2.012
R(C1–H3)	1.084	1.086	1.088	*R*(C1–H3)	1.084	1.085	1.088	*R*(C1–H3)	1.083	1.085	1.088
R(C2–O1)	1.420	1.431	1.421	*R*(C2–O1)	1.419	1.430	1.420	*R*(C2–O1)	1.422	1.433	1.423
R(C2–H4)	1.085	1.085	1.087	*R*(C2–H4)	1.085	1.085	1.087	*R*(C2–H4)	1.085	1.085	1.087
R(C2–H5)	1.090	1.090	1.092	*R*(C2–H5)	1.090	1.090	1.092	*R*(C2–H5)	1.090	1.090	1.092
R(C2–H6)	1.092	1.092	1.094	*R*(C2–H6)	1.092	1.092	1.094	*R*(C2–H6)	1.091	1.092	1.094
R(O2–H2)	0.977	0.985	0.984	*R*(O2–H2)	0.988	0.996	0.996	*R*(N–H2)	1.047	1.054	1.063
R(O2–N)	1.367	1.415	1.378	*R*(O2–N)	1.345	1.380	1.350	*R*(O2–N)	1.203	1.224	1.208
R(O3–N)	1.168	1.177	1.170	*R*(O3–N)	1.178	1.192	1.182	*R*(O3–N)	1.207	1.229	1.213
A(H1–C1–O1)	114.0	113.0	113.3	*A*(H1–C1–O1)	114.0	113.0	113.2	*A*(H1–C1–O1)	114.3	113.1	113.4
A(H1–C1–H2)	93.0	95.7	96.9	*A*(H1–C1–H2)	90.6	93.2	94.5	*A*(H1–C1–H2)	94.2	99.0	99.5
A(H1–C1–H3)	120.7	120.1	120.2	*A*(H1–C1–H3)	120.7	120.1	120.1	*A*(H1–C1–H3)	121.1	120.1	120.0
A(H3–C1–O1)	118.2	117.9	118.0	*A*(H3–C1–O1)	118.3	117.9	118.0	*A*(H3–C1–O1)	118.5	118.0	118.1
A(H2–C1–O1)	96.8	103.1	103.9	*A*(H2–C1–O1)	96.6	104.4	106.6	*A*(H2–C1–O1)	84.6	97.0	99.7
A(C1–O1–C2)	115.2	115.2	115.5	*A*(C1–O1–C2)	115.2	115.1	115.5	*A*(C1–O1–C2)	115.4	115.3	115.7
A(C1–H2–O2)	166.2	174.6	173.4	*A*(C1–H2–O2)	169.1	169.2	170.4	*A*(C1–H2–N)	143.6	162.8	163.8
A(H2–O2–N)	103.6	102.4	103.2	*A*(H2–O2–N)	107.9	107.7	108.4	*A*(H2–N–O2)	117.4	117.0	117.2
A(O2–N–O3)	111.7	111.7	111.9	*A*(O2–N–O3)	114.0	114.1	114.2	*A*(O2–N–O3)	127.6	127.3	127.2
D(H4–C2–O1–C1)	− 179.5	175.9	177.2	*D*(H4–C2–O1–C1)	− 177.3	177.6	178.7	*D*(H4–C2–O1–C1)	174.7	− 176.9	− 178.4
D(C2–O1–C1–H2)	93.4	85.4	83.0	*D*(C2–O1–C1–H2)	97.7	88.8	85.9	*D*(C2–O1–C1–H2)	− 103.5	− 85.6	− 82.6
D(O1–C1–H2–O2)	− 19.2	− 30.0	− 43.6	*D*(O1–C1–H2–O2)	75.4	127.0	130.5	*D*(O1–C1–H2–N)	42.4	35.8	36.7
D(C1–H2–O2–N)	− 27.4	− 13.0	− 1.8	*D*(C1–H2–O2–N)	− 121.6	− 176.2	171.5	*D*(C1–H2–N–O2)	− 150.7	− 162.6	− 163.6
D(H2–O2–N–O3)	179.4	179.8	179.8	*D*(H2–O2–N–O3)	− 0.8	0.1	0.2	*D*(C1–H2–N–O3)	29.2	17.6	16.4
$I_A I_B I_C$	10,664,807	12,633,284	11,490,773	$I_A I_B I_C$	8,888,190	10,842,077	10,298,341	$I_A I_B I_C$	8,122,293	10,723,476	10,101,152

[a]Bond lengths are in Å, bond and dihedral angles are in degrees, and products of principal moments of inertia are in amu^3 Å^6

Table 7 Comparison of scaled DFT ZPEs and experimental ZPEs (in kJ mol^{-1}) for species of reaction of DME with NO_2

Species	Experiment	BMK	M052X	M05	M062X	M06	M06L	B2PLYP	B2PLYPD	mPW2PLYP	mPW2PLYPD	wB97X	wB97XD
DME	203.10	205.37	205.09	204.97	205.44	204.07	204.41	206.85	207.04	208.51	208.22	205.04	205.17
NO_2	22.05	22.83	23.33	23.69	23.41	23.44	22.80	22.21	22.20	22.55	22.55	23.37	23.23
trans-HONO	50.74	53.42	53.30	53.61	53.46	53.40	51.87	51.30	51.32	52.14	52.13	53.36	53.34
cis-HONO	51.05	53.47	53.13	53.21	55.21	53.22	51.76	51.26	51.16	52.07	52.00	53.24	53.14
CH_3OCH_2	–	169.01	168.62	168.15	169.12	167.53	168.72	171.61	171.33	172.44	172.24	169.42	169.71
HNO_2	–	57.50	57.54	57.18	57.81	56.90	56.32	56.22	56.18	56.91	56.88	57.60	57.44
TSa	–	219.09	217.65	215.95	218.23	214.82	215.34	219.34	219.19	220.25	220.11	217.81	217.97
TSb	–	218.30	217.23	216.85	217.98	216.34	216.02	218.32	218.00	219.82	219.58	217.92	218.22
TSc	–	219.94	219.00	219.28	219.83	219.08	218.55	220.91	220.89	222.37	222.32	220.48	220.63
IMa	–	228.82	227.38	227.16	228.51	226.95	226.24	227.97	227.87	229.69	229.62	228.38	228.84
IMb	–	228.77	226.70	226.28	228.25	227.47	225.21	227.25	226.99	228.92	228.73	227.86	228.28
IMc	–	231.92	230.93	230.51	231.81	229.50	228.05	234.91	236.60	236.14	236.94	231.72	231.77
MUE	–	2.04	1.98	2.13	2.70	1.80	0.97	1.17	1.20	2.08	1.99	2.02	1.98

R(a), R(b), and R(c), which correspond to the difference between the energy of the saddle point and that of the reactants on the vibrationally adiabatic ground-state potentials for these reactions, $\Delta_f E_a$. The same procedure can be done for the reverse processes of reactions R(a), R(b), and R(c) to obtain $\Delta_r E_a$. These values calculated by various DFT methods for both the forward and reverse reactions are given in Table 8.

According to our calculated results collected in Table 8, the difference in the barrier heights among the three channels to form *trans*-HONO, *cis*-HONO, and HNO_2 can be probably ascribed to the difference in the structures among *trans*-HONO, *cis*-HONO, and HNO_2. These barrier heights indicate that only the two lower channels might be important at low temperatures since a decrease by 4.184 kJ mol^{-1} in the activation barriers will result in a remarkable increase in the rate constants by a factor of about 5. On the other hand, significant discrepancies are observed in the computed activation barriers, depending on the theoretical approach employed, i.e. the activation barriers without the ZPE corrections are predicted to lie in the range of 105–130 kJ mol^{-1} for R(a), 76–98 kJ mol^{-1} for R(b), and 81–99 kJ mol^{-1} for R(c), which points out the difficulty of obtaining an accurate energetic description of the title reaction.

In this regard, we add ZPE contributions to our best estimates of the zero-point-exclusive barrier heights obtained using coupled cluster single-point energy approximations at geometries optimized with the M06-2X/MG3S, B2PLYP/TZVP, and wB97XD/TZVP levels. The calculated results are outlined in Table 9. Scaling the ZPEs computed with the various DFT-based electronic model chemistries in Table 7 for the reactants and products resulted in anharmonic ZPEs that are in good agreement with experiment, indicating that the scaled ZPEs computed with these electronic model chemistries for the transition states should also be reliable.

It is satisfactory to observe from Table 9 that, with the basis set size and treatment of triple excitation, the CCSD(T)/6-311+G(2df,2p), CCSD(T)/aug-cc-pVTZ, CCSD(T)/CBS, and QCISD(T)/6-311+G(2df,2p) computed activation barriers based on the optimized structures at the M06-2X/MG3S, B2PLYP/TZVP, and wB97XD/TZVP levels agree very well, and match well with the double-HDFT calculated results in Table 8. From Table 9, we can also find the activation barriers for the three reaction channels are predicted to be in the $\Delta_f E_a$[R(a)] > $\Delta_f E_a$[R(c)] > $\Delta_f E_a$[R(b)] order, indicating that the reaction R(b) to form *cis*-HONO is the most possible reaction channel for the hydrogen abstraction from DME by NO_2. However, the above energetic order is in contrary with the structural analysis based on the Hammond's postulate, which is also observed in the hydrogen abstractions R(a), R(b), and R(c) from the $-CH_3$ group of CH_3OH by the NO_2 radical [56].

Table 8 Computed barrier heights (in kJ mol^{-1}) by various DFT methods for the reaction of DME with NO_2

Electronic model chemistry	Forward barrier height ($\Delta_f E_a$)			Reverse barrier height ($\Delta_r E_a$)		
	R(a)	R(b)	R(c)	R(a)	R(b)	R(c)
BMK/MG3S	113.34 (122.45)[a]	80.16 (90.06)	92.88 (101.14)	59.12 (68.84)	24.14 (34.61)	6.89 (18.87)
MPW1K/MG3S	123.29 (135.23)	93.14 (103.45)	92.80 (101.13)	62.26 (73.89)	29.63 (38.60)	10.03 (21.20)
MPWB1K/MG3S	124.59 (135.98)	93.18 (103.83)	96.96 (105.55)	61.75 (72.37)	29.06 (38.92)	9.29 (20.91)
MPW3LYP/MG3S	102.67 (114.15)	73.51 (84.27)	80.71 (89.22)	45.25 (55.78)	13.44 (22.52)	0.02 (10.78)
M05/MG3S	123.03 (135.74)	90.19 (102.01)	92.11 (101.49)	52.71 (63.92)	18.40 (27.84)	5.56 (16.79)
M052X/MG3S	119.56 (130.78)	83.25 (94.44)	87.63 (97.05)	70.55 (80.73)	34.30 (43.79)	10.52 (22.44)
M06/MG3S	111.10 (123.28)	83.46 (94.58)	86.98 (95.40)	52.57 (64.18)	21.64 (32.71)	5.02 (15.43)
M062X/MG3S	112.70 (123.32)	78.92 (89.79)	89.06 (98.09)	65.67 (75.95)	31.29 (41.55)	8.61 (20.59)
M06L/MG3S	105.33 (117.20)	80.92 (92.11)	88.42 (97.08)	28.05 (38.95)	2.19 (11.38)	− 4.29 (5.20)
B2PLYP/TZVP	129.01 (138.63)	94.19 (105.53)	98.84 (107.58)	60.75 (69.68)	20.47 (29.40)	1.67 (15.67)
B2PLYPD/TZVP	125.72 (135.78)	88.66 (99.90)	94.01 (102.36)	59.71 (68.39)	18.48 (27.47)	1.18 (15.52)
mPW2PLYP/TZVP	127.06 (137.88)	91.56 (102.80)	97.07 (105.77)	62.74 (72.18)	23.43 (32.53)	4.07 (17.84)
mPW2PLYPD/TZVP	123.72 (134.38)	87.50 (98.70)	93.51 (101.96)	61.82 (71.32)	22.01 (31.16)	2.43 (17.05)
wB97X/TZVP	116.00 (126.59)	85.15 (95.64)	93.50 (101.44)	60.94 (71.51)	27.51 (37.45)	9.59 (20.83)
wB97XD/TZVP	112.94 (123.37)	81.45 (91.63)	87.66 (95.44)	54.16 (65.03)	19.49 (29.55)	3.42 (14.56)

ZPEs are scaled

[a]Values in parentheses exclude ZPE corrections

Furthermore, the following functional form [57] is employed to predict the position of the first-order saddle point

$$x_0^* = 1/\left[2 - \left(\Delta E/\Delta E_a\right)\right] \quad (2)$$

x_0^* ($0 \le x_0^* \le 1$) in Eq. (2) which corresponds to the calculated result of the reaction coordinate for the first-order saddle point; ΔE and ΔE_a denote the reaction energy and the activation energy, respectively. The calculated results for x_0^* are presented in Table 10. The reactions R(a), R(b), and R(c) are all endothermic with $\Delta E > 0$. x_0^* for TSa, TSb, and TSc are calculated to be 0.680, 0.821, and 0.983 with the B2PLYP/TZVP-based results, respectively, greater than 0.5. It can be argued that the three transition structures for the reaction DME with NO_2 should approach the post-reaction adducts with the higher energy content, which is contrary to the fact that both TSa and TSb are located to be reactant-like by quantum chemical calculations.

Although *trans*-HONO is the lowest energy HNO_2 isomer, followed by *cis*-HONO, then HNO_2, the barrier heights are highest for the *trans*-HONO channel, and lowest for the formation of *cis*-HONO with that for the production of HNO_2 being in between. This behavior can be partly attributed to the stabilizing effect of a seven-member ring in the TSc structure for HNO_2 formation and an eight-member ring in the TSb structure for *cis*-HONO formation, as recommended by Chan et al. [8]. In addition, given that *trans*-HONO is more stable than *cis*-HONO by only about 2 kJ mol^{-1}, one would expect the barrier height for R(a) to be close to that for R(b). However, this value is predicted to be about 37 kJ mol^{-1} much higher. This chemical behavior can be elucidated by the molecular orbitals of NO_2, as suggested by Chai and Goldsmith [58]. One of the two nodal planes of the singularly occupied molecular orbital of NO_2 centers on each oxygen atom, and the other centers on the nitrogen atom. When the DME molecule comes close to the N end of NO_2, it overlaps with only one lobe. As DME heads either oxygen atom from the *cis*-direction, it mostly overlaps with the positive oxygen-centered lobe with minimal mixing of the negative lobe, but heading the *trans*-direction, the DME molecule suffers almost equivalent positive and negative overlaps in face of the oxygen-centered nodal plane, making for a closer CH_3OCH_2H–ONO distance to ensure enough overlap which gives rise to extra Coulombic repulsion, and then the activation barrier for reaction R(a) grows. In addition, based on geometrical parameters shown in Tables 4 and 5, one can see that the reactive N···O bond in the TSa geometry is stretched more to take part in the O···H bond being formed compared to that in the TSb geometry, indicating the tendency to break the N···O π bond for TSa, which is confirmed by the B2PLYP/TZVP calculated Mulliken spin densities on the reactive O atoms to form the O···H bonds of TSa and TSb by 0.64 e and 0.30 e, respectively. Here it should be pointed out that, compared to channel R(b), the geometry of NO_2 fragment exhibits large change besides the C···H being broken and O···H being formed bonds in R(a), leading to that the unpaired electron is transferred to the O atom to take part in the formation of the O···H bond, which provides an essential contribution to increasing the energetics of TSa.

Table 9 Computed barrier heights (in kJ mol^{-1}) based on coupled cluster theory extrapolated to CBS limit and composite methods for the reaction of DME with NO_2

Electronic model chemistry	Forward barrier height ($\Delta_r E_a$)			Reverse barrier height ($\Delta_r E_a$)		
	R(a)	R(b)	R(c)	R(a)	R(b)	R(c)
CCSD/6-311+G(2df,2p)//M062X/MG3S	145.33 (155.95)[a]	102.10 (112.96)	108.66 (117.68)	98.00 (108.28)	52.13 (62.39)	24.14 (36.12)
CCSD(T)/6-311+G(2df,2p)//M062X/MG3S	130.08 (140.70)	95.69 (106.56)	101.62 (110.64)	75.26 (85.53)	38.32 (48.58)	15.46 (27.44)
CCSD(T)/aug-cc-pVTZ//M062X/MG3S	130.06 (140.68)	93.03 (103.90)	103.70 (112.72)	76.35 (86.63)	37.67 (47.93)	14.08 (26.06)
CCSD(T)/CBS//M062X/MG3S	129.96 (140.79)	95.33 (105.19)	100.99 (108.60)	77.32 (87.81)	38.88 (51.86)	15.39 (27.37)
QCISD(T)/6-311+G(2df,2p)//M062X/MG3S	129.90 (140.52)	94.25 (105.12)	101.39 (110.41)	74.35 (84.63)	36.04 (46.30)	14.28 (26.26)
CCSD/6-311+G(2df,2p)//B2PLYP/TZVP	145.46 (155.77)	97.77 (109.11)	106.03 (114.78)	100.21 (108.83)	50.41 (59.34)	20.00 (34.35)
CCSD(T)/6-311+G(2df,2p)//B2PLYP/TZVP	131.03 (141.34)	95.17 (106.51)	101.08 (109.82)	77.58 (86.20)	39.12 (48.05)	12.85 (27.19)
CCSD(T)/aug-cc-pVTZ//B2PLYP/TZVP	130.84 (141.15)	92.90 (104.24)	103.93 (112.67)	78.70 (87.32)	39.15 (48.08)	12.35 (26.69)
CCSD(T)/CBS//B2PLYP/TZVP	130.76 (141.57)	93.12 (104.94)	99.96 (108.71)	79.20 (88.23)	39.27 (49.64)	12.72 (27.07)
QCISD(T)/6-311+G(2df,2p)//B2PLYP/TZVP	130.76 (141.07)	93.76 (105.10)	101.19 (109.93)	76.70 (85.32)	36.79 (45.73)	11.83 (26.17)
CCSD/6-311+G(2df,2p)//wB97XD/TZVP	139.43 (149.86)	100.96 (111.14)	108.58 (116.35)	91.16 (102.03)	49.89 (59.94)	23.55 (34.69)
CCSD(T)/6-311+G(2df,2p)//wB97XD/TZVP	130.04 (142.48)	96.32 (106.50)	101.50 (110.27)	76.40 (87.34)	37.80 (47.85)	13.98 (27.26)
CCSD(T)/aug-cc-pVTZ//wB97XD/TZVP	130.44 (142.95)	93.89 (104.07)	103.94 (112.71)	77.23 (88.18)	37.79 (47.85)	15.51 (26.65)
CCSD(T)/CBS//wB97XD/TZVP	130.00 (140.50)	94.72 (104.92)	100.40 (108.18)	77.47 (88.89)	38.18 (49.02)	14.90 (26.18)
QCISD(T)/6-311+G(2df,2p)//wB97XD/TZVP	130.30 (140.74)	95.31 (105.49)	102.39 (110.16)	74.07 (84.94)	36.03 (46.09)	15.09 (26.23)
CBS-QB3	130.56	88.25	97.86	71.59	25.23	12.33
G3B3	127.12	88.31	99.03	71.76	28.86	12.20
G3MP2B3	127.47	88.65	100.23	73.09	30.01	13.01
G4	125.88	91.31	97.14	72.59	31.09	13.58
G4MP2	123.06	88.09	96.24	73.88	35.23	14.49

ZPEs are scaled

[a]Values in parentheses exclude ZPE corrections

Unfortunately, there is no experimentally derived activation barrier for each channel of the NO_2 + DME reaction for comparison. Even the calculated barrier heights forming *cis*-HONO (the lowest barrier channel) in this work are approximately 20 kJ mol^{-1} higher than the experimental result [6] of 73.64 kJ mol^{-1}. Here we compare the calculated activation energies for the title reaction with those of similar reaction systems. The activation barriers for the hydrogen abstractions from the $-CH_3$ group of CH_3OH by the NO_2 radical were predicted to be 89.54 kJ mol^{-1} in the temperature range 639–713 K by Anastasi and Hancock [59] and 89.54 kJ mol^{-1} at temperatures from 900 to 1100 K by Koda and Tanaka [60], respectively. From the above, one can see that our calculated activation energies for the title reaction match well with the previously reported estimates of similar systems.

Comparison of barriers for bimolecular NO_2 + DME reaction versus C–O bond fission of DME (the dissociation barrier for C–O bond was previously computed to be 339 kJ mol^{-1} [61]), suggests that the bimolecular process should enhance the combustion rate of DME and shifts the temperature for the initial oxidation to lower values. In addition, activation barrier for the title reaction is also predicted to be less than that for the bimolecular O_2 + DME reaction [62], indicating that the DME combustion can be initiated at a lower temperature by the reaction of DME with NO_2 seeded in the DME–O_2–NO_2 system compared to the DME/O_2 interactions without NO_2, which was observed experimentally by Alzueta et al. [5].

Table 10 Characterization of transition states for the reaction of DME with NO_2

Electronic model chemistry	x_0^{*a}		
	TSa	TSb	TSc
M062X/MG3S	0.632	0.716	0.912
CCSD(T)/6-311+G(2df,2p)//M062X/MG3S	0.633	0.714	0.868
CCSD(T)/aug-cc-pVTZ//M062X/MG3S	0.630	0.712	0.880
CCSD(T)/CBS//M062X/MG3S	0.627	0.710	0.868
QCISD(T)/6-311+G(2df,2p)//M062X/MG3S	0.636	0.723	0.876
B2PLYP/TZVP	0.680	0.821	0.983
CCSD(T)/6-311+G(2df,2p)//B2PLYP/TZVP	0.628	0.709	0.887
CCSD(T)/aug-cc-pVTZ//B2PLYP/TZVP	0.624	0.704	0.894
CCSD(T)/CBS//B2PLYP/TZVP	0.623	0.703	0.887
QCISD(T)/6-311+G(2df,2p)//B2PLYP/TZVP	0.630	0.718	0.895
wB97XD/TZVP	0.676	0.807	0.962
CCSD(T)/6-311+G(2df,2p)//wB97XD/TZVP	0.630	0.718	0.879
CCSD(T)/aug-cc-pVTZ//wB97XD/TZVP	0.628	0.713	0.870
CCSD(T)/CBS//wB97XD/TZVP	0.626	0.713	0.871
QCISD(T)/6-311+G(2df,2p)//wB97XD/TZVP	0.638	0.726	0.872
CBS-QB3	0.646	0.778	0.888
G3B3	0.639	0.754	0.890
G3MP2B3	0.636	0.747	0.885
G4	0.634	0.746	0.877
G4MP2	0.625	0.714	0.869

[a] x_0^* is the value of the defined reaction coordinate for the transition state

3.5 Zero-point-corrected reaction energies

The calculated energies of separate products and post-reaction complex relative to the separate reactants NO_2 + DME are summarized in Tables 11 and 12, respectively. The energy of separate reactants NO_2 + DME is set as zero for reference.

From Table 11, one can see that the three reaction channels are all predicted to be endothermic. The M06-2X/MG3S-based computations provide a zero-point-corrected reaction enthalpy of 70.01 kJ mol^{-1} for R(a), 70.28 kJ mol^{-1} for R(b), and 107.86 kJ mol^{-1} for R(c) at 298 K, respectively, being in excellent accordance with the experimental estimations of 73.27 kJ mol^{-1} for R(a), 75.21 kJ mol^{-1} for R(b), and 106.33 kJ mol^{-1} for R(c), respectively, by employing these experimentally based enthalpies of formation given by $\Delta H_{f,298}^{\circ}$ (CH_3OCH_3) = −184.01 kJ mol^{-1}, $\Delta H_{f,298}^{\circ}$ (NO_2) = 34.039 kJ mol^{-1}, and $\Delta H_{f,298}^{\circ}$ (*trans*-HONO) = −78.675 kJ mol^{-1} in Ref. [63]; $\Delta H_{f,298}^{\circ}$ (*cis*-HONO) = −76.73 kJ mol^{-1} and $\Delta H_{f,298}^{\circ}$ (HNO_2) = −45.61 ± 0.2 kJ mol^{-1} in Ref. [64]; $\Delta H_{f,298}^{\circ}$ (CH_3OCH_2) = 1.97 kJ mol^{-1} in Ref. [65].

Here it should be noted that B2PLYP/TZVP, which will be used for the future kinetics calculations based on the good performance for geometry optimizations, ZPEs, and zero-point-inclusive barrier heights, overestimates these values by about 15 kJ mol^{-1} with regard to the experimental values, and the wB97XD/TZVP level also overestimates these values by about 10 kJ mol^{-1}. Table 11 also shows that if the CCSD(T)/6-311+G(2df,2p), CCSD(T)/aug-cc-pVTZ, CCSD(T)/CBS, and QCISD(T)/6-311+G(2df,2p) single-point energies are employed, the computed reaction enthalpies with the ZPE corrections based on the optimized structures at the M06-2X/MG3S, B2PLYP/TZVP, and wB97XD/TZVP levels are in reasonable agreement and compare very well with the experimental reaction enthalpies at 298 K with gap less than 3 kJ mol^{-1}. The computationally less demanding CCSD(T)/6-311+G(2df,2p) can reproduce the results of the CBS limit for the energetics of the present reaction system. Thus the less expensive CCSD(T)/6-311+G(2df,2p) method was chosen for the subsequent chemical kinetic analysis of ignition characteristics of DME. Comparing Tables 9 and 11, one can observe that the separate products CH_3OCH_2 + HNO_2 lie higher in energy by about 8 kJ mol^{-1} than the identified transition state TSc, implying that TSc cannot be directly linked to them.

Table 12 presents the calculated energies of three post-reaction complexes located between the transition states and final separate products for reactions R(a), R(b), and R(c). From Table 12, we found that the CCSD(T) and QCISD(T) evaluations give very close energies of intermediates relative to reactants CH_3OCH_3 + NO_2, and the basis set superposition errors involved in the present theoretical study are very small. IMc is predicted to lie by 15 kJ mol^{-1} in energy lower than TSc, and this value is reduced to 10 kJ mol^{-1} when the BSSE corrections are considered.

Depending on the discussions above, the theoretical compound method CCSD(T)/6-311+G(2df,2p)//B2PLYP/TZVP will be chosen to conduct chemical kinetic analysis of the DME/NO_2 reaction system.

4 Conclusions

Quantum chemical calculations were performed on the three reaction channels of DME with the NO_2 radical to form *trans*-HONO, *cis*-HONO, and HNO_2, respectively. It was found that the hydrogen abstractions proceeded with NO_2 preferentially attacking the out-of-plane hydrogen atoms of DME. Each channel involved the formation of a van der Waals post-reaction complex lying below the corresponding transition state and separate products in energy. Single-reference formalisms were argued to reliably characterize the systems considered here, and "double-hybrid" density functionals B2PLYP, B2PLYPD, mPW2PLYP, and mPW2PLYPD in conjunction with the TZVP basis set have been found to give accurate geometries and principal moments of inertia

Table 11 Computed reaction energies and enthalpies (ΔE and ΔH in kJ mol^{-1}) based on separate products relative to separate reactants for the reaction of DME with NO_2

Electronic model chemistry	R(a)		R(b)		R(c)	
	ΔE	ΔH	ΔE	ΔH	ΔE	ΔH
M062X/MG3S	69.14 (74.31)[a]	70.01	69.25 (74.28)	70.28	107.40 (108.32)	107.86
CCSD(T)/6-311+G(2df,2p)//M062X/MG3S	72.49 (78.52)	73.52	74.03 (80.20)	74.90	108.10 (110.01)	108.55
CCSD(T)/aug-cc-pVTZ//M062X/MG3S	68.84 (74.86)	69.87	70.43 (76.60)	71.30	106.30 (108.22)	106.76
CCSD(T)/CBS//M062X/MG3S	69.43 (75.46)	70.46	70.97 (77.14)	71.84	105.54 (107.46)	106.00
QCISD(T)/6-311+G(2df,2p)//M062X/MG3S	73.27 (79.29)	74.30	75.00 (81.17)	75.87	109.18 (111.10)	109.64
B2PLYP/TZVP	85.38 (92.08)	86.46	88.98 (95.77)	89.84	115.27 (117.09)	115.55
CCSD(T)/6-311+G(2df,2p)//B2PLYP/TZVP	72.04 (78.74)	73.12	73.63 (80.41)	74.49	108.58 (110.40)	108.86
CCSD(T)/aug-cc-pVTZ//B2PLYP/TZVP	68.02 (74.73)	69.11	69.83 (76.61)	70.69	106.81 (108.64)	107.10
CCSD(T)/CBS//B2PLYP/TZVP	68.43 (75.14)	69.51	69.97 (76.76)	70.83	106.99 (108.82)	107.27
QCISD(T)/6-311+G(2df,2p)//B2PLYP/TZVP	72.61 (79.32)	73.69	74.62 (79.32)	75.48	109.93 (111.75)	110.21
wB97XD/TZVP	81.29 (86.64)	82.31	83.71 (89.26)	84.54	112.09 (113.35)	112.46
CCSD(T)/6-311+G(2df,2p)//wB97XD/TZVP	72.94 (78.29)	73.95	74.70 (80.25)	75.53	108.96 (110.22)	109.34
CCSD(T)/aug-cc-pVTZ//wB97XD/TZVP	69.20 (74.55)	70.22	71.06 (76.61)	71.89	107.19 (108.44)	107.56
CCSD(T)/CBS//wB97XD/TZVP	69.73 (75.08)	70.74	71.46 (77.01)	72.29	106.28 (107.54)	106.66
QCISD(T)/6-311+G(2df,2p)//wB97XD/TZVP	73.65 (79.00)	74.66	75.68 (81.23)	76.51	110.12 (111.38)	110.49
CBS-QB3	77.43	78.51	79.26	80.12	110.99	111.33
G3B3	73.22	74.23	75.97	76.75	107.54	107.84
G3MP2B3	70.74	71.75	73.76	74.54	108.32	108.63
G4	72.60	73.58	75.29	76.06	106.32	106.63
G4MP2	69.43	70.40	72.28	73.05	106.50	106.80

ZPEs are scaled

[a]Values in parentheses exclude ZPE corrections

Table 12 Computed energies (ΔE in kJ mol^{-1}) of post-reaction complex relative to the separate reactants for the reaction of DME with NO_2

Electronic model chemistry	IMa		IMb		IMc	
	ΔE	ΔH	ΔE	ΔH	ΔE	ΔH
M062X/MG3S	47.03 (48.46)[a]	48.88 (50.44)	47.12 (48.24)	48.76 (50.02)	80.46 (81.75)	81.85 (83.53)
CCSD(T)/6-311+G(2df,2p)//M062X/MG3S	54.82 (58.77)	56.67 (60.74)	57.35 (60.53)	58.99 (62.32)	86.16 (90.30)	87.56 (92.08)
CCSD(T)/aug-cc-pVTZ//M062X/MG3S	53.71 (59.46)	55.56 (61.44)	54.74 (58.80)	56.38 (60.58)	88.62 (93.19)	90.01 (94.97)
CCSD(T)/CBS//M062X/MG3S	54.42 (58.98)	56.37 (60.93)	54.96 (58.20)	56.59 (59.83)	88.58 (92.90)	89.97 (94.29)
QCISD(T)/6-311+G(2df,2p)//M062X/MG3S	55.55 (59.51)	57.40 (61.49)	58.19 (61.40)	59.83 (63.19)	87.11 (91.26)	88.50 (93.04)
B2PLYP/TZVP	69.26 (72.50)	71.54 (74.88)	73.72 (76.71)	75.87 (76.88)	97.17 (99.75)	98.62 (101.28)
CCSD(T)/6-311+G(2df,2p)//B2PLYP/TZVP	53.45 (57.48)	55.73 (59.85)	56.04 (60.22)	58.20 (62.38)	88.23 (92.10)	89.70 (93.63)
CCSD(T)/aug-cc-pVTZ//B2PLYP/TZVP	52.14 (58.06)	54.42 (60.44)	55.90 (60.75)	58.05 (62.90)	89.58 (94.18)	91.05 (95.71)
CCSD(T)/CBS//B2PLYP/TZVP	52.46 (57.02)	54.31 (58.86)	56.66 (60.39)	58.21 (61.93)	89.52 (93.30)	90.83 (94.60)
QCISD(T)/6-311+G(2df,2p)//B2PLYP/TZVP	54.05 (58.03)	56.33 (60.30)	56.96 (61.16)	59.11 (63.31)	89.36 (93.88)	90.83 (95.36)
wB97XD/TZVP	58.77 (60.71)	60.31 (62.39)	61.96 (64.04)	63.25 (65.24)	84.24 (85.96)	85.24 (86.98)
CCSD(T)/6-311+G(2df,2p)//wB97XD/TZVP	55.57 (59.72)	57.11 (61.26)	58.52 (63.27)	59.81 (64.56)	86.38 (91.09)	87.38 (92.09)
CCSD(T)/aug-cc-pVTZ//wB97XD/TZVP	54.21 (60.39)	55.75 (61.93)	56.10 (61.58)	57.38 (62.87)	89.43 (94.90)	90.43 (95.91)
CCSD(T)/CBS//wB97XD/TZVP	54.59 (59.14)	56.13 (60.67)	54.78 (61.95)	58.07 (63.24)	89.36 (93.51)	90.38 (94.52)
QCISD(T)/6-311+G(2df,2p)//wB97XD/TZVP	56.24 (60.52)	57.77 (62.21)	59.28 (64.34)	60.56 (65.55)	87.29 (92.10)	88.30 (93.11)

ΔE and ΔH include ZPE corrections and ZPEs are scaled

[a]Values in parentheses include BSSE corrections

of reactants and products. In particular, the B2PLYP/TZVP level could provide results for zero-point-inclusive barriers comparable in accuracy to the accurate CCSD(T) and QCISD(T) calculations while decreasing the computational time substantially. Finally, we found that it was unnecessary to drive the CCSD(T) theory extrapolated to the CBS limit from aug-cc-pVDZ and aug-cc-pVTZ basis sets with regard to the calculations of energetics involved in the reactions of DME with NO_2. The CCSD(T) and QCISD(T) methods accompanied by the aug-cc-pVTZ and 6-311+G(2df,2p) basis sets based on the M06-2X/MG3S, B2PLYP/TZVP, and wB97XD/TZVP geometries could also produce results of benchmarking quality. Therefore, the computationally affordable CCSD(T)/6-311+G(2df,2p)//B2PLYP/TZVP electronic model chemistry will be employed to perform the kinetic modeling of the three reaction channels of DME with the NO_2, and for the investigations of homologous reaction systems, the use of the proposed electronic model chemistry is also highly suggested.

Acknowledgements This work was supported by the National Natural Science Foundation of China (No. 21606178).

References

1. Kohse-Höinghaus K, Oßwald P, Cool TA, Kasper T, Hansen N, Qi F, Westbrook CK, Westmoreland PR (2010) Biofuel combustion chemistry: from ethanol to biodiesel. Angew Chem Int Ed 49:3572–3597
2. Ribeiro NM, Pinto AC, Quintella CM, da Rocha GO, Teixeira LSG, Guarieiro LLN, do Carmo Rangel M, Veloso MCC, Rezende MJC, da Cruz RS, de Oliveira AM, Torres EA, de Andrade JB (2007) The role of additives for diesel and diesel blended (ethanol or biodiesel) fuels: a review. Energy Fuels 21:2433–2445
3. Arcoumanis C, Bae C, Crookes R, Kinoshita E (2008) The potential of di-methyl ether (DME) as an alternative fuel for compression-ignition engines: a review. Fuel 87:1014–1030
4. Miller JA, Bowman CT (1989) Mechanism and modeling of nitrogen chemistry in combustion. Prog Energy Combust Sci 15:287–338
5. Alzueta MU, Muro J, Bilbao R, Glarborg P (1999) Oxidation of dimethyl ether and its interaction with nitrogen oxides. Isr J Chem 39:73–86
6. Dagaut P, Lucheke J, Cathonnet M (2001) The low temperature oxidation of DME and mutual sensitization of the oxidation of DME and nitric oxide: experimental and detailed kinetic modeling. Combust Sci Technol 165:61–84
7. Ye W, Shi JC, Zhang RT, Wu XJ, Zhang X, Qi ML, Luo SN (2016) Experimental and kinetic modeling study of CH_3OCH_3 ignition sensitized by NO_2. Energy Fuels 30:10900–10908
8. Chan WT, Heck SM, Pritchard HO (2001) Reaction of nitrogen dioxide with hydrocarbons and its influence on spontaneous ignition. A computational study. Phys Chem Chem Phys 3:56–62
9. Frisch MJ, Trucks GW, Schlegel HB, Scuseria GE, Robb MA, Cheeseman JR, Scalmani G, Barone V, Mennucci B, Petersson GA et al (2009) Gaussian 09, revision A.02. Gaussian, Inc., Wallingford
10. Boese AD, Martin JML (2004) Development of density functionals for thermochemical kinetics. J Chem Phys 121:3405–3416
11. Lynch BJ, Fast PL, Harris M, Truhlar DG (2000) Adiabatic connection for kinetics. J Phys Chem A 104:811–4815
12. Zhao Y, Truhlar DG (2004) Hybrid meta density functional theory methods for thermochemistry, thermochemical kinetics, and noncovalent interactions: the MPW1B95 and MPWB1K models and comparative assessments for hydrogen bonding and van der Waals interactions. J Phys Chem A 108:6908–6918
13. Chai JD, Head-Gordon M (2008) Systematic optimization of long-range corrected hybrid density functional. J Chem Phys 128:084106/1–15
14. Chai JD, Head-Gordon M (2008) Long-range corrected hybrid density functionals with damped atom–atom dispersion corrections. Phys Chem Chem Phys 10:6615–6620
15. Zhao Y, Schultz NE, Truhlar DG (2005) Exchange-correlation functional with broad accuracy for metallic and nonmetallic compounds, kinetics, and noncovalent interactions. J Chem Phys 123:161103/1–4
16. Zhao Y, Schultz NE, Truhlar DG (2006) Design of density functionals by combining the method of constraint satisfaction with parameterization for thermochemistry, thermochemical kinetics, and noncovalent interactions. J Chem Theory Comput 2:364–382
17. Zhao Y, Truhlar DG (2006) Comparative DFT study of van der Waals complexes: rare-gas dimers, alkaline-earth dimers, zinc dimer, and zinc-rare-gas dimmers. J Phys Chem A 110:5121–5129
18. Zhao Y, Truhlar DG (2008) The M06 suite of density functionals for main group thermochemistry, thermochemical kinetics, noncovalent interactions, excited states, and transition elements: two new functionals and systematic testing of four M06-class functionals and 12 other functionals. Theor Chem Acc 120:215–241
19. Zhao Y, Truhlar DG (2006) A new local density functional for main-group thermochemistry, transition metal bonding, thermochemical kinetics, and noncovalent interactions. J Chem Phys 125:194101/1–18
20. Schäfer A, Huber C, Ahlrichs R (1994) Fully optimized contracted gaussian basis sets of triple zeta valence quality for atoms Li to Kr. J Chem Phys 100:5829–5835
21. Lynch BJ, Zhao Y, Truhlar DG (2003) Effectiveness of diffuse basis functions for calculating relative energies by density functional theory. J Phys Chem A 107:1384–1388
22. Zheng J, Zhao Y, Truhlar DG (2009) The DBH24/08 database and its use to assess electronic structure model chemistries for chemical reaction barrier heights. J Chem Theory Comput 5:808–821
23. Zhao Y, Truhlar DG (2008) Density functionals with broad applicability in chemistry. Acc Chem Res 41:157–167
24. Grimme S (2006) Semiempirical hybrid density functional with perturbative second-order correlation. J Chem Phys 124:034108/1–16
25. Schwabe T, Grimme S (2007) Double-hybrid density functionals with long-range dispersion corrections: higher accuracy and extended applicability. Phys Chem Chem Phys 9:3397–3406
26. Grimme S, Antony J, Ehrlich S, Krieg H (2010) A consistent and accurate ab initio parametrization of density functional dispersion correction (DFT-D) for the 94 elements H-Pu. J Chem Phys 132:154104/1–19
27. Grimme S (2011) Density functional theory with london dispersion corrections. Wiley Interdiscip Rev Comput Mol Sci 1:211–228
28. Schwabe T, Grimme S (2006) Towards chemical accuracy for the thermodynamics of large molecules: new hybrid density functionals including non-local correlation effects. Phys Chem Chem Phys 8:4398–4401

29. Hratchian HP, Schlegel HB (2004) Accurate reaction paths using a Hessian based predictor–corrector integrator. J Chem Phys 120:9918–9924
30. Hratchian HP, Schlegel HB (2005) Using Hessian updating to increase the efficiency of a Hessian based predictor–corrector reaction path following method. J Chem Theory Comput 1:61–69
31. Purvis GD III, Bartlett RJ (1982) A full coupled-cluster singles and doubles model: the inclusion of disconnected triples. J Chem Phys 76:1910–1918
32. Scuseria GE, Janssen CL, Schaefer HF III (1988) An efficient reformulation of the closed-shell coupled cluster single and double excitation (CCSD) equations. J Chem Phys 89:7382–7387
33. Gauss J, Cremer D (1988) Analytical evaluation of energy gradients in quadratic configuration-interaction theory. Chem Phys Lett 150:280–286
34. Pople JA, Head-Gordon M, Raghavachari K (1987) Quadratic configuration interaction—a general technique for determining electron correlation energies. J Chem Phys 87:5968–5975
35. Dunning TH Jr (1989) Gaussian basis sets for use in correlated molecular calculations. I. The atoms boron through neon and hydrogen. J Chem Phys 90:1007–1023
36. Kendall RA, Dunning TH Jr, Harrison RJ (1992) Electron affinities of the first-row atoms revisited. Systematic basis sets and wave functions. J Chem Phys 96:6796–6806
37. Woon DE, Dunning TH Jr (1993) Gaussian basis sets for use in correlated molecular calculations. III. The atoms aluminum through argon. J Chem Phys 98:1358–1371
38. Schwenke DW (2005) The extrapolation of one-electron basis set in electronic structure calculations: how it should work and how it can be made to work. J Phys Chem 122:014107/1–7
39. Baboul AG, Curtiss LA, Redfern PC, Raghavachari K (1999) Gaussian-3 theory using density functional geometries and zero-point energies. J Chem Phys 110:7650–7657
40. Montgomery JA Jr, Frisch MJ, Ochterski JW, Petersson GA (1999) A complete basis set model chemistry. VI. Use of density functional geometries and frequencies. J Chem Phys 110:2822–2827
41. Curtiss LA, Redfern PC, Raghavachari K (2007) Gaussian-4 theory. J Chem Phys 126:084108/1–12
42. Curtiss LA, Redfern PC, Raghavachari K (2007) Gaussian-4 theory using reduced order perturbation theory. J Chem Phys 127:124105/1–8
43. Boys SF, Bernardi F (1970) Calculation of small molecular interactions by differences of separate total energies-some procedures with reduced errors. Mol Phys 19:553–566
44. Lee TJ, Taylor PR (1989) A diagnostic for determining the quality of single-reference electron correlation methods. Int J Quantum Chem 23:199–207
45. Zhao Y, Tishchenko O, Gour JR, Li W, Lutz JJ, Piecuch P, Truhlar DG (2009) Thermochemical kinetics for multireference systems: addition reactions of ozone. J Phys Chem A 113:5786–5799
46. Karton A, Rabinovich E, Martin JML, Ruscic B (2006) W4 theory for computational thermochemistry: in pursuit of confident sub-kJ/mol predictions. J Chem Phys 125:144108/1–17
47. Rienstra-Kiracofe JC, Allen WD, Schaefer HF III (2000) The $C_2H_5 + O_2$ reaction mechanism: high-level ab initio characterizations. J Phys Chem A 104:9823–9840
48. Peiró-García J, Nebot-Gil I (2003) Ab initio study of the mechanism of the atmospheric reaction: $NO_2 + O_3 \rightarrow NO_3 + O_2$. J Comput Chem 24:1657–1663
49. Peiró-García J, Nebot-Gil I (2003) Ab initio study on the mechanism of the atmospheric reaction $OH + O_3 \rightarrow HO_2 + O_2$. ChemPhysChem 4:843–847
50. Lambert N, Kaltsoyannis N, Price SD, Žabka J, Herman Z (2006) Bond-forming reactions of dications with molecules: a computational and experimental study of the mechanisms for the formation of HCF^{2+} from CF_3^{2+} and H_2. J Phys Chem A 110:2898–2905
51. Feller D, Peterson KA, Dixon DA (2008) A survey of factors contributing to accurate theoretical predictions of atomization energies and molecular structures. J Chem Phys 129:204105/1–32
52. Sullivan MB, Iron MA, Redfern PC, Martin JML, Curtiss LA, Radom L (2003) Heats of formation of alkali metal and alkaline earth metal oxides and hydroxides: surprisingly demanding targets for high-level ab initio procedures. J Phys Chem A 107:5617–5630
53. Johnson III RD (2018) Computational chemistry comparison and benchmark database, version 18; National Institute of Standards and Technology. http://cccbdb.nist.gov/. Accessed 19 Oct 2018
54. Alecu IM, Zheng J, Zhao Y, Truhlar DG (2010) Computational thermochemistry: scale factor databases and scale factors for vibrational frequencies obtained from electronic model chemistries. J Chem Theory Comput 6:2872–2887
55. Kesharwani MK, Brauer B, Martin JML (2015) Frequency and zero-point vibrational energy scale factors for double-hybrid density functionals (and other selected methods): can anharmonic force fields be avoided? J Phys Chem A 119:1701–1714
56. Xiao CX, Yan N, Zou M, Hou SC, Kou Y, Liu W, Zhang S (2006) NO_2-catalyzed deep oxidation of methanol: experimental and theoretical studies. J Mol Catal A Chem 252:202–211
57. Miller AR (1978) A theoretical relation for the position of the energy barrier between initial and final states of chemical reactions. J Am Chem Soc 100:1984–1992
58. Chai J, Goldsmith CF (2017) Rate coefficients for fuel + NO_2: predictive kinetics for HONO and HNO_2 formation. Proc Combust Inst 36:617–626
59. Anastasi C, Hancock DU (1988) NO_2 kinetic studies using laser-induced fluorescence. J Chem Soc Faraday Trans 2 84(10):1697–1706
60. Koda S, Tanaka M (1986) Ignition of premixed methanol/air in a heated flow tube and the effect of NO_2 addition. Combust Sci Technol 47:165–176
61. Tranter RS, Lynch PT, Yang X (2013) Dissociation of dimethyl ether at high temperatures. Proc Combust Inst 34:591–598
62. Guan Y, Gao J, Song Y, Li Y, Ma H, Song J (2017) Variational effect and anharmonic torsion on kinetic modeling for initiation reaction of dimethyl ether combustion. J Phys Chem A 121:1121–1132
63. Ruscic B, Bross DH (2018) Active Thermochemical Tables (ATcT) Values Based on Version 1.122 of the Thermochemical Network. ATcT.anl.gov. Accessed 15 Dec 2018
64. Asatryan R, Bozzelli JW, Simmie JM (2007) Thermochemistry for enthalpies and reaction paths of nitrous acid isomers. Int J Chem Kinet 39:378–398
65. Guan Y, Lou J, Liu R, Ma H, Song J (2018) Thermodynamic properties of the methylmethoxy radical with intricate treatment of two-dimensional hindered internal rotations. J Chem Eng Data 63:3640–3649